
Article:
Kulak, AN orcid.org/0000-0002-2798-9301, Grimes, R, Kim, Y-Y orcid.org/0000-0002-8503-4554 et al. (5 more authors) (2016) Polymer-Directed Assembly of Single Crystal Zinc Oxide/ Magnetite Nanocomposites under Atmospheric and Hydrothermal Conditions. Chemistry of Materials, 28 (20). pp. 7528-7536. ISSN 0897-4756

https://doi.org/10.1021/acs.chemmater.6b03563

Polymer-Directed Assembly of Single Crystal Zinc Oxide/ Magnetite Nanocomposites under Atmospheric and Hydrothermal Conditions

Alexander N. Kulak[a], Rebecca Grimes[a], Yi-Yeoun Kim[a], Mona Semsarilar[b], Clara Anduix-Canto[a], Oscar Cespedes[c], Steven P. Armes[b] and Fiona C. Meldrum[a*]

[a]School of Chemistry, University of Leeds, Woodhouse Lane, Leeds, LS2 9JT, UK.

[b]Dainton Building, Department of Chemistry, University of Sheffield, Brook Hill, Sheffield, Yorkshire, S3 7HF, UK.

[c]School of Physics and Astronomy, University of Leeds, Woodhouse Lane, Leeds, LS2 9JT, UK.

ABSTRACT: Within the field of crystal growth it is recognized that secondary species can sometimes be occluded within a growing crystal according to the crystallization conditions and pairing of the additive and host crystal. This article takes inspiration from this phenomenon to create multifunctional inorganic nanocomposites with unique structures – inorganic single crystals containing embedded inorganic nanoparticles. Using magnetite (Fe_3O_4)/ ZnO as a suitable test system, ZnO crystals are precipitated from aqueous solution at 90 ^{o}C and atmospheric pressure in the presence of Fe_3O_4 nanoparticles functionalized with anionic diblock copolymers. Analysis of product nanocomposite crystals using atomic absorption spectroscopy shows that the Fe_3O_4 nanoparticles are embedded within the ZnO single crystal hosts at levels of approximately 10 wt%, while TEM analysis shows that there is no apparent discontinuity between the nanoparticles and host crystal matrix. Importantly, we then demonstrate that this occlusion approach can also be employed under hydrothermal conditions at 160 ^{o}C, without a loss in occlusion efficiency. This offers an important advance on our previous occlusion studies, which were all conducted at room temperature, and vastly increases the range of target materials that can be generated using our synthesis approach. Finally, measurement of the magnetic properties of these nanocomposites shows that they retain the attractive features of the wide band-gap semiconductor ZnO, while benefiting from added magnetism.

INTRODUCTION

Effective routes for fabricating inorganic nanocomposites promise the ability to engineer the compositions, structures and properties of materials at the nanoscale and mesoscale, creating multi-functionality and potentially even novel properties.[1] A range of approaches have been used to construct nanocomposites, including traditional methods such as mechanical mixing and annealing, which gives relatively poor control over the nanostructure, or vapor phase deposition processes which are commonly used to generate lamellar-type structures.[2, 3] Spinodal decomposition can generate nanoparticles within a crystalline matrix, but it is difficult to precisely control the size, distribution and shapes of such occlusions.[4] More complex geometries can be formed via top-down processing or templating,[5] and chemical solution processing can be used to create materials such as thin films incorporating metal NPs.[6, 7] Nanocomposites can also be formed via the assembly of pre-formed nanoparticles, where random networks of nanoparticles have been created as gels or aerogels,[8-10] and ordered structures can be generated as nanoparticle superlattices.[11, 12] These structures promise interesting properties including tunable conductivity[13] and enhanced energy transfer.[14]

This article describes an alternative strategy for synthesizing inorganic nanocomposites with unique structures; embedding inorganic nanoparticles within inorganic single crystals. The occlusion of nanoparticles within single crystals rather than amorphous or polycrystalline matrices has the potential to generate a new class of materials, where the elimination of grain boundaries can enhance properties such as conductivity,[15] optical[16] or mechanical properties.[17] Indeed, superior properties were observed even on embedding quantum dots within the individual domains of polycrystalline organo-perovskites.[18] Further, by encapsulating the nanoparticles within a single crystal host, they are also entirely isolated/ protected from the environment. A number of methods have been used to occlude inorganic nanoparticles within single crystals, including the coprecipitation of NaCl with quantum dots functionalised with short chain thiols,[19, 20] or MOFs with nanoparticles functionalized with a non-ionic hydrophilic polymer, poly(*N*-vinylpyrrolidone) (PVP).[21] Alternatively, calcite ($CaCO_3$) has been precipitated in the presence of gels impregnated with nanoparticles.[22, 23] All of these approaches tend to give relatively low levels of occlusion.

Inspired by the composite structures of single crystal biominerals, in which proteins are embedded within the crystal lattice,[24, 25] we have developed an alternative approach in which particles functionalized with copolymer chains are used as simple growth additives. Using the common biomineral calcite as a host crystal, early work demonstrated that organic particles functionalized with surface chains can be occluded

within calcite single crystals at levels as high as 30 vol%.[17, 26, 27] We then extended this strategy to occlude block copolymer-functionalized inorganic nanoparticles within calcite.[28, 29]

The current study demonstrates that this assembly-based method can also be employed to generate multi-functional inorganic nanocomposites. Using ZnO/ magnetite (Fe_3O_4) as a suitable model system, we show that magnetite nanoparticles functionalized with a poly(methacrylic acid)-poly(potassium 3-sulfopropyl methacrylate) (PMAA-PKSPMA) diblock copolymer (Figure 1a) are occluded within the ZnO wurtzite lattice at levels of 10 wt% under typical aqueous reaction conditions at 90 ^{o}C. We also make an important advance in our assembly-based synthesis strategy by demonstrating for the first time that it can also be employed under hydrothermal conditions; near identical occlusion levels were achieved when the ZnO/ magnetite nanocomposites were synthesized under hydrothermal conditions at 160 ^{o}C. These experiments demonstrate that this copolymer-directed occlusion strategy provides a novel and effective means for synthesizing inorganic nanocomposites, where access to hydrothermal conditions opens the door to the synthesis of a wide range of functional materials.

RESULTS

ZnO was selected for study as it can be formed as micron-scale crystals under moderate reaction conditions (aqueous solution, < 100 ^{o}C), which enables us to clearly demonstrate that the associated nanoparticles are occluded within the crystals rather than adsorbed to their surfaces, and because this semiconductor attracts significant attention as a potential cheap, transparent, conducting oxide with a band gap in the near UV.[30-32] By then incorporating magnetite (Fe_3O_4) nanoparticles within ZnO we combine two materials with contrasting functionalities, where ZnO/ Fe_3O_4 nanocomposites have attracted interest due to possible applications in areas including optoelectronic and spintronic devices,[33-36] photocatalysis,[37-39] cancer immunotherapy,[40] water detoxification,[41] and microwave absorption.[42]

The double-hydrophilic diblock copolymer PMAA-PKSPMA (Figure 1a) was selected as a suitable stabilizer for the magnetite nanoparticles (MNPs) and was synthesized using reversible addition-fragmentation chain transfer (RAFT) polymerization.[43] The PMAA block was prepared first in ethanol at 70 °C using ACVA initiator and a trithiocarbonate-based RAFT agent (see Experimental). After purification via dialysis, the near-monodisperse $PMAA_{23}$ precursor was chain-extended using KSPMA in aqueous solution, with essentially full conversion being achieved within 18 h at 70 °C. The carboxylate-functionalized PMAA block was expected to bind strongly to the magnetite, and the sulfonate-functionalized chains to form a corona

around the MNPs. The PKSPMA block then acts as an electrosteric stabilizer, ensuring the colloidal stability of the MNPs in the crystal growth solution, and enables their strong binding to the growing ZnO crystals and thus their occlusion within the ZnO lattice. That binding of the block copolymer to the magnetite particles occurs via the PMAA block was demonstrated by the relatively weak pH-dependence of the zeta potential of the copolymer-stabilized particles, which is consistent with the strongly acidic PKSPMA block acting as the stabilizer block. Naked magnetite sols, by comparison, exhibited positive zeta potentials from pH 2 to 7, negative zeta potentials from pH 7 to 12 and an isoelectric point at pH z 7 (see Figure S1).

Block copolymer-functionalized magnetite nanoparticles (PS-MNPs) were then generated on precipitation of magnetite (Fe_3O_4) in the presence of the PMAA-PKSPMA copolymer using established methods (Figure 1a). That the nanoparticles were magnetite was confirmed by powder-XRD (p-XRD) (Figure S2), while transmission electron microscopy (TEM) analysis showed that they had mean diameters of 4 – 10 nm (Figure 1b). High resolution TEM (Figure 1c) and electron diffraction (Figure 1d) also confirmed that the nanocrystals were magnetite. In making this analysis it is noted that these diffraction-based techniques cannot distinguish between magnetite and maghemite.[44] However, the black color of the nanoparticles and their Raman spectra suggest that the particles are principally magnetite. Thermogravimetric analysis (TGA) was used to investigate their compositions, and showed that the PS-MNPs underwent a 6.8 wt% loss up to 200 ^{o}C, which is attributed to dehydration, and a further 36.7 wt% loss up to 550 ^{o}C, which is attributed to copolymer pyrolysis (Figure S3). This shows that the PS-MNPs comprise 37 wt% copolymer PMAA-PKSPM, 56 wt% Fe_3O_4 and 7 wt % water, and demonstrates the presence of a substantial copolymer shell around the inorganic nanoparticles.

Having generated suitable copolymer-functionalized nanoparticles, we then investigated their occlusion within ZnO crystals, where ZnO was precipitated from aqueous solution at 90 ^{o}C in the presence of hexamethyltetramine (HMTA) using established protocols.[45] Initial control experiments were performed over a range of solution compositions in the absence of the copolymer-stabilized MNPs (PS-MNPs), and crystalline ZnO with the wurtzite structure was generated in all cases, as confirmed by powder XRD (Figure S2). Morphological examination of the crystals using scanning electron microscopy (SEM) showed that the sizes and degrees of aggregation of the rods varied according to the concentration of HMTA and Zn^{2+}[46] in the reaction solution (Figure 2). The rods had lengths of 3.36 μm (SD 0.55) and aspect ratios of 6-8 at [Zn^{2+}] = [HMTA] = 0.5 mM (Figure 2a), and lengths of 3.43 μm (SD 0.62) and aspect ratios of 7-10 at [Zn^{2+}] = [HMTA] = 1 mM (Figure 2b). They were principally non-aggregated under both sets of conditions and the

rods formed at reagent concentrations of 1 mM were particularly uniform in size. Further increase in the $[Zn^{2+}]$ = [HMTA] to 1.5mM led to the formation of flower-like bundles of individual rods of 1.6 μm (SD 0.35) in length (Figure 2c), where a low magnification image is shown in Figure S4.

Addition of the PS-MNPs to the ZnO precipitation caused significant changes in the sizes and shapes of the ZnO crystals (Figure 3), while p-XRD confirmed that they were still wurtzite. A change from rod-like to barrel-shaped occurred on addition of 0.168 mg mL^{-1} PS-MNPs to reactions of composition $[Zn^{2+}]$ = [HMTA] = 0.5 mM, such that the crystals were ≈ 0.53 μm (SD 0.086) in length and 0.31 μm (SD 0.046) in diameter and exhibited highly roughened surfaces (Figure 3a). Doubling the concentration of PS-MNPs to 0.336 mg mL^{-1} resulted in the formation of small hexagonal crystals with a broad range of diameters (0.4 – 1 μm) (Figure 3b), while a further increase to 0.504 mg mL^{-1} PS-MNPs generated a film of ZnO crystallites (Figure S5). The reaction conditions were therefore further varied to obtain well-defined ZnO particles in the presence of the PS-MNPs. Holding the concentration of PS-MNPs constant at 0.168 mg mL^{-1} while increasing $[Zn^{2+}]$ = [HMTA] to 1 mM gives 1.015 μm (SD 0.2) × 0.357 (SD 0.049) μm rods with significantly smoother surfaces than those generated at $[Zn^{2+}]$ = [HMTA] = 0.5 mM (Figure 3c), while further increase to $[Zn^{2+}]$ = [HMTA] = 1.5 mM generated marginally larger rods of sizes 2 × 0.5 μm (Figure S6). Precipitation of ZnO in the presence of the highest concentration of PS-MNPs (0.504 mg mL^{-1}) at $[Zn^{2+}]$ = [HMTA] = 1.0 mM and 1.5 mM failed to yield any improvement in particle uniformity, and flake-like particles of ZnO were produced (Figure 3d and Figure S7). This pattern of morphological changes mirrors that seen on coprecipitation of ZnO with carboxylated latex particles,[45, 47] where blocking of growth along the *c*-axis by the particle additives causes a reduction in aspect ratio and ultimate formation of flake-like particles.

The ZnO/PS-MNP nanocomposite crystals were then subjected to detailed characterization to determine the efficiency of occlusion, and the location of the occluded PS-MNPs within the ZnO crystal matrix. Atomic absorption (AA) analysis was used to quantify the amounts of MNPs occluded, where this was conducted after cleaning the surfaces of the ZnO/PS-MNP particles to remove any adsorbed nanoparticles; the values determined therefore correspond to NPs occluded within the ZnO crystals only. While AA analysis after sonicating the ZnO/PS-MNP crystals in water yielded a value of 16 ± 2 wt % polymer-coated nanoparticles in the nanocomposites, AA of crystals that had been sonicated in 10 % sodium hypochlorite for 30 min yielded a value of 10 wt% PS-MNPs. This indicates the surface adsorption of PS-MNPs, where these are removed via oxidative decomposition of the copolymer by the hypochlorite. This procedure is standard practice to remove surface-bound and intracrystalline organic molecules from biominerals.[48] The

nanocomposite crystals were also characterized using Raman microscopy, where the resultant spectrum is shown in Figure S8a, together with spectra for the PS-MNPs, pure ZnO and the copolymer. The ZnO/PS-MNP crystals exhibit the ZnO E2 modes at 330 and 437 cm^{-1},[49] together with the principal peak for magnetite at 667 cm^{-1},[50] and bands from the polymer at 637 and 798 cm^{-1}. It is noted that iron oxides and oxyhydroxides are poor light scatterers,[51] such that the magnetite peak is of low intensity as compared with the ZnO peaks. Magnetite also readily converts to haematite under irradiation with the Raman laser (Figure S8b).[50, 51] The spectrum of maghemite is distinct from that of magnetite, showing clear peaks at 350, 512 and 664 cm^{-1}.[50, 51]

Individual nanocomposite crystals were analyzed by TEM to determine their location within the ZnO crystals. Crystals precipitated under reagent concentrations of $[Zn^{2+}]$ = [HMTA] = 0.5 mM and 0.336 mg mL^{-1} PS-MNPs were selected for analysis as these hexagonal crystals are sufficiently thin for analysis (Figure 4a). Selected area electron diffraction (SAED) of individual particles confirmed that they were single crystals of ZnO (Figure 4b) and that they contained magnetite. Weak scattering spots corresponding to the occluded magnetite (311) were observed when the crystals were tilted off-zone using a double-tilt holder; this procedure reduces the intensity of diffraction from the majority ZnO phase (Figure 4c). The corresponding TEM images of the nanocomposite crystals then revealed the locations of the MNPs within the ZnO lattice (Figure 4d). While the similarity in atomic number of Fe and Zn means that they exhibit similar contrast in the TEM, particles 4 – 10 nm in size corresponding to the MNPs can be clearly seen within the ZnO. High resolution TEM (HRTEM) images were also recorded and showed that the MNPs are embedded within the ZnO matrix with no apparent loss in the continuity of the ZnO lattice (Figure 4e).

Having demonstrated that our one-pot method can be used to achieve efficient occlusion of inorganic nanoparticles under moderate reaction conditions, we then extended our study to investigate whether this strategy remains viable under hydrothermal conditions. Not only do ZnO particles precipitated under hydrothermal conditions exhibit superior properties to their counterparts synthesized at lower-temperatures,[52] but hydrothermal synthesis also opens the door to a wide range of functional materials that cannot be formed at moderate conditions. These experiments were conducted for 12 h at 160 ^{o}C in a Teflon bomb, using reagent concentrations of $[Zn^{2+}]$ = [HMTA] = 5 mM. Large, acicular ZnO crystals as bundles of rods 7 μm (SD 1.4) in length were generated in control experiments in the absence of PS-MNPs (Figure 5a), while addition of PS-MNPs at 3.36 mg mL^{-1} induced the formation of 2.35 μm (SD 0.54) particles with well-defined, double-barrelled morphologies (Figure 5b).

The crystals were then characterized to determine the efficiency of PS-MNP occlusion under these more extreme conditions. Atomic absorption demonstrated occlusion of ≈ 9 wt% PS-MNPs after hypochlorite-treatment, where this is comparable to the ≈ 10 wt% achieved under the standard conditions. Samples for TEM analysis were prepared by grinding the crystals to create a fragment thin enough for analysis (Figure 6a). SAED of this sample clearly showed rings corresponding to magnetite superimposed on a ZnO single crystal pattern (Figure 6b) and bright field imaging revealed the presence of nanoparticle occlusions within the ZnO lattice (Figure 6c). Finally, dark field imaging was performed, where the magnetite nanoparticle diffracting as the circled rings in Figure 6b become clearly visible (Figure 6d).

Finally, the magnetic properties of the ZnO/PS-MNP nanocomposite crystals were investigated using a vibrating sample magnetometer (SQUID-VSM) with a sensitivity > 10^{-8} emu over the temperature range 2 K to 350 K. Analysis of the copolymer-stabilized magnetite nanoparticles (PS-MNPs) and the ZnO/ PS-MNP nanocomposite crystals (produced under "standard conditions" at 90 ^{o}C and under hydrothermal conditions) showed that all samples are superparamagnetic at room temperature, exhibit saturation magnetizations of 3-4 emu g^{-1} and become ferromagnetic, with zero coercivity, below the blocking temperature (Figure 7). However, differing blocking temperatures were observed. The PS-MNPs and standard ZnO/PS-MNP samples have values of 92 ± 2 K, in good agreement with reported studies of 10 nm diameter Fe_3O_4 nanoparticles.[53] In contrast, the samples prepared using the hydrothermal method had a blocking temperature of just 53 K. The blocking temperature is proportional to the product of the magnetic anisotropy, *K1*, and the particle volume, *V*. Given that the particle size does not change, this implies a change in magnetic anisotropy of 40 %, which would lead to a *K1* value of ≈ 2.7 x 10^5 erg/cc.[53] This is consistent with an improvement in the quality of the magnetite nanoparticles on heating under hydrothermal conditions, as is also suggested by the observed changes in magnetization of this sample.

Looking then at the magnetization curves (Figure 8), the PS-MNPs have a net magnetization of 44 emu g^{-1} Fe_3O_4 at low temperatures and fields of 5 T, where this is calculated based on a composition of 56 wt% Fe_3O_4. This is not far from the 80 emu g^{-1} reported in the literature for 10 nm crystalline Fe_3O_4 nanoparticles, as measured at low temperatures.[53] The lower value recorded here suggests that the magnetite nanoparticles employed here are poorly crystalline, as is often observed for synthesis in the presence of polymers, and they may also exhibit an Fe_2O_3 surface layer which can cause magnetization changes.[54] The ZnO/PS-MNP crystals synthesized at 90°C (which comprise 10 wt% PS-MNPs and thus 5.6

wt% Fe_3O_4) have a magnetization of 38 emu g^{-1} Fe_3O_4, which indicates little change in the magnetite nanoparticles on occlusion in the ZnO at 90 °C. For the nanocomposite crystals synthesized by the hydrothermal method, however, we obtain a significantly higher value of 62 emu g^{-1} Fe_3O_4 (where these comprise 9 wt% PS-MNPs and thus 5.0 wt% Fe_3O_4), which is very close to the values reported for high quality spherical particles of a similar size.[53] The higher magnetization in hydrothermal samples may be due to an improved structure achieved via the higher synthesis temperature of 160° C. The low temperature coercivity H_C is proportional to the ratio of the anisotropy over the saturation magnetization: $\mathrm{H_C} \propto \mathrm{K/M_S}$. A 40% lower anisotropy and 50% higher magnetisation for the hydrothermal samples should lead to a 60-70% lower coercivity. This is consistent with the low temperature hysteresis loops (insets in Figure 8), which show an H_C of 25 mT for copolymer/standard samples and 10 mT for samples prepared via the hydrothermal method.

DISCUSSION

A wide range of approaches have been used to create nanocomposites based on ZnO. Nanoparticle and ZnO formation can be performed simultaneously, such as in the creation of thin films of ZnO nanorods decorated with metal nanoparticles using vapor-deposition methods,[55] or the use of solid state annealing of Zn and Fe_2O_3 to generate Fe_3O_4 nanoparticles embedded in a ZnO film.[35] Solvothermal and hydrothermal routes have been employed to generate ZnO rods supporting Ag nanoparticles,[56] and hollow Ag/ZnO microspheres respectively,[57] while mixed ZnO/CuO "mesocrystal" nanocomposites were formed on annealing the metal precursor solutions with an amphiphilic triblock copolymer.[58] Multi-step processes have been used to generate nanoparticles with well-defined core/shell structures, such as Fe_2O_3/ZnO,[59] and Fe_3O_4/ZnO,[37] while a range of core/shell structures have been formed on partial conversion of ZnO microspheres. Nanoparticles can also be precipitated on the surfaces of pre-synthesized ZnO, such as Au on mesoporous ZnO particles.[60] In all of these methods it can be challenging to achieve control over the size and properties of the associated nanoparticles. This problem can be overcome by the adsorption of pre-made nanoparticles to the ZnO,[37] or alternatively, co-precipitation in the presence of pre-made nanoparticles. The latter route was used to occlude glycine-functionalized Fe_3O_4 nanoparticles in polycrystalline ZnO microspheres, leading to effective loading.[41]

The strategy demonstrated here – in which we embed inorganic nanoparticles within a single crystal host via a one-pot method – is a relatively unexplored route to generating inorganic nanocomposites. This approach offers the advantages that we employ pre-synthesized nanoparticles, such that we can profit

from the vast knowledge that is available about controlling nanoparticle synthesis, and that we occlude the nanoparticles within a single crystal lattice. With the absence of grain boundaries, this can also to lead to an enhancement of properties such as electrical conductivity.[15] The nanoparticles are also entirely isolated within the host crystal lattice, preventing their exposure to the environment.

Considering then the incorporation of "occlusion species" within single crystals in more detail, this phenomenon has been recognized for hundreds of years in the ability to color certain single crystals with partner dye molecules.[61] A further well-studied example is offered by the field of biomineralization, where single crystal calcite and aragonite biominerals invariably occlude biomacromolecules at levels of ≈ 0.1-1 wt%.[62] Building on these observations, recent work has shown that certain amino acids can be occluded within synthetic calcite crystals,[63, 64] and ZnO,[65] and labelled biomolecules in calcium oxalate.[66] Particle occlusion during solution-phase crystallization, by comparison, is currently only recognized in a few crystal systems, including quantum dots/ NaCl or borax (with quite low levels of occlusion),[19, 20] Au nanoparticles/ MOFs,[21] and organic and inorganic nanoparticles in calcite ($CaCO_3$).[17, 26-29] It is also well-established that poly(styrene-acrylic acid) latex nanoparticles, prepared by miniemulsion polymerization, can be effectively occluded within ZnO single crystals.[45, 47] Similar occlusion has also been obtained using sulfate-based anionic diblock copolymer nanoparticles.[67]

Insight into the mechanism by which the particles become occluded into single crystals has only been obtained for the calcite system, where *in situ* AFM was used to image the occlusion of block copolymer micelles. The nanoparticles were seen to bind specifically to the step edges (negligible binding to the terraces is observed), which then experience little or no inhibition by the adsorbed micelles.[68] Further, the micelles experience significant compression during occlusion, which generates local lattice strain and the formation of a transient cavity. AFM has also been used to show that calcite grows around islands of stearic acid molecules adsorbed to planar {104} faces, thereby incorporating them into the crystal lattice.[69] That these particles can be occluded while not affecting crystal growth may simply be dependent on the concentration of the additive used. Indeed, aspartic acid is very efficiently occluded at low concentrations,[63] but gives no signature of this behavior in the crystal morphology or AFM growth studies until higher concentrations are reached.

While the growth of calcite is well-characterized, many questions remain concerning the growth of ZnO. The last few decades have seen huge advances in our understanding of crystal growth mechanisms, and it

is now recognized that many (insoluble) nanoparticles grow via non-classical mechanisms based on the oriented aggregation of precursor particles.[70] Studies of the growth of ZnO crystals have suggested that it can grow both via classical and non-classical routes, depending on the experimental conditions.[71, 72] Precipitation from alcohol solutions,[71, 72] or aqueous solution in the presence of organic additives[73] have provided strong evidence of aggregation-based growth, while analysis of growth kinetics in solution has also provided a good fit to classical models of crystal growth.[46, 74] Based on the literature it is therefore not possible to identify the mechanism by which ZnO grows in the two sets of experiments performed here. However, given that the product crystals are micron-scale, it is likely that the much of the growth occurs under a classical regime and that the particles are occluded via binding to step edges or even terraces in a similar mechanism to that operating in the calcite system.

CONCLUSIONS

Inorganic nanocomposites comprising Fe_3O_4 (magnetite) nanoparticles embedded within a ZnO single crystal host can be generated using a simple, one-pot method in which copolymer-functionalized nanoparticles are employed as simple crystal growth additives in reactions performed in aqueous solution at 90 ^{o}C. Importantly, we also show for the first time that effective occlusion can still be achieved under hydrothermal conditions at 160 ^{o}C for 12 h. Our previous body of work focused on the formation of occlusions ranging from 200 nm particles to organic and inorganic nanoparticles to small molecules within calcite ($CaCO_3$), where calcite was selected as a suitable model system as it is well-recognized to readily occlude various additives, including biomacromolecules[75] and gels.[76] The reported successful extension of our approach to a functional host crystal and more extreme hydrothermal reaction conditions therefore suggests that our strategy could be applied to a range of inorganic/inorganic nanocomposite single crystals.

ASSOCIATED CONTENT

Supporting Information. The experimental methods and additional characterization data of the nanocomposite crystals is provided in the Supporting Information. This material is available free of charge via the Internet at http://pubs.acs.org.

Data Availability. The data that support the findings of this study are available in the "Research Data Leeds Repository" with the identifier http://doi.org/xxxx.[77]

AUTHOR INFORMATION

Corresponding Author

*Fiona Meldrum, email F.Meldrum@leeds.ac.uk. Tel +44 113 3436414.

Author Contributions

The manuscript was written through contributions of all authors.

ACKNOWLEDGMENT

We thank the EPSRC for financial support via grants EP/G00868X/1 (AK and FCM), EP/J018589/1 (YYK and FCM) and EP/K006304/1 (AK, FCM, LAF and SPA). This work was also supported by an EPSRC Leadership Fellowship (EP/H005374/1; FCM and YYK) and an ERC Advanced Investigator grant (PISA 320372; SPA).

REFERENCES

1. Nan, C.-W.; Jia, Q., Obtaining Ultimate Functionalities in Nanocomposites: Design, Control and Fabrication. *MRS Bull.* **2015,** *40*, 719.

2. Biswas, K.; He, J. Q.; Zhang, Q. C.; Wang, G. Y.; Uher, C.; Dravid, V. P.; Kanatzidis, M. G., Strained endotaxial nanostructures with high thermoelectric figure of merit. *Nature Chem.* **2011,** *3*, 160.

3. Heron, J. T.; Trassin, M.; Ashraf, K.; Gajek, M.; He, Q.; Yang, S. Y.; Nikonov, D. E.; Chu, Y. H.; Salahuddin, S.; Ramesh, R., Electric-Field-Induced Magnetization Reversal in a Ferromagnet-Multiferroic Heterostructure. *Phys. Rev. Letts.* **2011,** *107*, 5.

4. Johnsen, S.; He, J. Q.; Androulakis, J.; Dravid, V. P.; Todorov, I.; Chung, D. Y.; Kanatzidis, M. G., Nanostructures Boost the Thermoelectric Performance of PbS. *J. Am. Chem. Soc.* **2011,** *133*, 3460.

5. Aimon, N. M.; Choi, H. K.; Sun, X. Y.; Kim, D. H.; Ross, C. A., Templated Self-Assembly of Functional Oxide Nanocomposites. *Adv. Mater.* **2014,** *26*, 3063.

6. Bahlawane, N.; Kohse-Hoinghaus, K.; Weimann, T.; Hinze, P.; Rohe, S.; Baumer, M., Rational Design of Functional Oxide Thin Films with Embedded Magnetic or Plasmonic Metallic Nanoparticles. *Angew. Chem. Int. Ed.* **2011,** *50*, 9957.

7. Walters, G.; Parkin, I. P., The incorporation of noble metal nanoparticles into host matrix thin films: synthesis, characterisation and applications. *J. Mater. Chem.* **2009,** *19*, 574.

8. Gaponik, N.; Wolf, A.; Marx, R.; Lesnyak, V.; Schilling, K.; Eychmuller, A., Three-Dimensional Self-Assembly of Thiol-Capped CdTe Nanocrystals: Gels and Aerogels as Building Blocks for Nanotechnology. *Adv. Mater.* **2008,** *20*, 4257.

9. Cai, B.; Wen, D.; Liu, W.; Herrmann, A. K.; Benad, A.; Eychmuller, A., Function-Led Design of Aerogels: Self-Assembly of Alloyed PdNi Hollow Nanospheres for Efficient Electrocatalysis. *Angew. Chem. Int. Ed.* **2015,** *54*, 13101.

10. Singh, A.; Lindquist, B. A.; Ong, G. K.; Jadrich, R. B.; Singh, A.; Ha, H.; Ellison, C. J.; Truskett, T. M.; Milliron, D. J., Linking Semiconductor Nanocrystals into Gel Networks through All-Inorganic Bridges. *Angew. Chem. Int. Ed.* **2015,** *54*, 14840.

11. Liu, W. Y.; Tagawa, M.; Xin, H. L. L.; Wang, T.; Emamy, H.; Li, H. L.; Yager, K. G.; Starr, F. W.; Tkachenko, A. V.; Gang, O., Diamond family of nanoparticle superlattices. *Science* **2016,** *351*, 582.

12. Kovalenko, M. V.; Manna, L.; Cabot, A.; Hens, Z.; Talapin, D. V.; Kagan, C. R.; Klimov, V. I.; Rogach, A. L.; Reiss, P.; Milliron, D. J.; Guyot-Sionnnest, P.; Konstantatos, G.; Parak, W. J.; Hyeon, T.; Korgel, B. A.; Murray, C. B.; Heiss, W., Prospects of Nanoscience with Nanocrystals. *ACS Nano* **2015,** *9*, 1012.

13. Cargnello, M.; Johnston-Peck, A. C.; Diroll, B. T.; Wong, E.; Datta, B.; Damodhar, D.; Doan-Nguyen, V. V. T.; Herzing, A. A.; Kagan, C. R.; Murray, C. B., Substitutional doping in nanocrystal superlattices. *Nature* **2015,** *524*, 450.

14. Cargnello, M.; Diroll, B. T.; Gaulding, E. A.; Murray, C. B., Enhanced Energy Transfer in Quasi-Quaternary Nanocrystal Superlattices. *Adv. Mater.* **2014,** *26*, 2419.

15. Crossland, E. J. W.; Noel, N.; Sivaram, V.; Leijtens, T.; Alexander-Webber, J. A.; Snaith, H. J., Mesoporous TiO2 single crystals delivering enhanced mobility and optoelectronic device performance. *Nature* **2013,** *495*, 215.

16. Popov, A. S.; Uklein, A. V.; Multian, V. V.; Le Dantec, R.; Kostenyukova, E. I.; Bezkrovnaya, O. N.; Pritula, I. M.; Gayvoronsky, V. Y., Nonlinear optical response of nanocomposites based on KDP single crystal with incorporated Al(2)O(3)(*)nH(2)O nanofibriles under CW and pulsed laser irradiation at 532 nm. *Optics Communications* **2016,** 379, 45.

17. Kim, Y. Y.; Ganesan, K.; Yang, P. C.; Kulak, A. N.; Borukhin, S.; Pechook, S.; Ribeiro, L.; Kroger, R.; Eichhorn, S. J.; Armes, S. P.; Pokroy, B.; Meldrum, F. C., An artificial biomineral formed by incorporation of copolymer micelles in calcite crystals. *Nature Mater.* **2011,** 10, (11), 890.

18. Ning, Z. J.; Gong, X. W.; Comin, R.; Walters, G.; Fan, F. J.; Voznyy, O.; Yassitepe, E.; Buin, A.; Hoogland, S.; Sargent, E. H., Quantum-dot-in-perovskite solids. *Nature* **2015,** *523*, 324.

19. Muller, M.; Kaiser, M.; Stachowski, G. M.; Resch-Genger, U.; Gaponik, N.; Eychmuller, A., Photoluminescence Quantum Yield and Matrix-Induced Luminescence Enhancement of Colloidal Quantum Dots Embedded in Ionic Crystals. *Chem. Mater.* **2014,** *26*, 3231.

20. Adam, M.; Erdem, T.; Stachowski, G. M.; Soran-Erdem, Z.; Lox, J. F. L.; Bauer, C.; Poppe, J.; Demir, L. V.; Gaponik, N.; Eychmuller, A., Implementation of High-Quality Warm-White Light-Emitting Diodes by a Model-Experimental Feedback Approach Using Quantum Dot-Salt Mixed Crystals. *ACS Appl. Mater. Int.* **2015,** *7*, 23364.

21. Lu, G.; Li, S. Z.; Guo, Z.; Farha, O. K.; Hauser, B. G.; Qi, X. Y.; Wang, Y.; Wang, X.; Han, S. Y.; Liu, X. G.; DuChene, J. S.; Zhang, H.; Zhang, Q. C.; Chen, X. D.; Ma, J.; Loo, S. C. J.; Wei, W. D.; Yang, Y. H.; Hupp, J. T.; Huo, F. W., Imparting functionality to a metal-organic framework material by controlled nanoparticle encapsulation. *Nature Chem.* **2012,** *4*, 310.

22. Kim, Y. Y.; Schenk, A. S.; Walsh, D.; Kulak, A. N.; Cespedes, O.; Meldrum, F. C., Bio-inspired formation of functional calcite/metal oxide nanoparticle composites. *Nanoscale* **2014,** *6*, 852.

23. Liu, Y. J.; Yuan, W. T.; Shi, Y.; Chen, X. Q.; Wang, Y.; Chen, H. Z.; Li, H. Y., Functionalizing Single Crystals: Incorporation of Nanoparticles Inside Gel-Grown Calcite Crystals. *Angew. Chem. Int. Ed.* **2014,** *53*, 4127.

24. Berman, A.; Addadi, L.; Kvick, A.; Leiserowitz, L.; Nelson, M.; Weiner, S., Intercalation of sea urchin protein in calcite: Study of a crystalline composite material. *Science* **1990,** 250, 664-667.

25. Dunlop, J. W. C.; Fratzl, P., Biological Composites. In *Ann. Rev. Mater. Res.*, Annual Reviews: Palo Alto, 2010; Vol. 40, pp 1-24.

26. Kim, Y. Y.; Ribeiro, L.; Maillot, F.; Ward, O.; Eichhorn, S. J.; Meldrum, F. C., Bio-Inspired Synthesis and Mechanical Properties of Calcite-Polymer Particle Composites. *Adv. Mater.* **2010,** *22*, 2082.

27. Kim, Y. Y.; Semsarilar, M.; Carloni, J. D.; Cho, K. R.; Kulak, A. N.; Polishchuk, I.; Hendley, C. T.; Smeets, P. J. M.; Fielding, L. A.; Pokroy, B.; Tang, C. C.; Estroff, L. A.; Baker, S. P.; Armes, S. P.; Meldrum, F. C., Structure and Properties of Nanocomposites Formed by the Occlusion of Block Copolymer Worms and Vesicles Within Calcite Crystals. *Adv. Func. Mater.* **2016,** *26*, 1382.

28. Kulak, A. N.; Semsarilar, M.; Kim, Y. Y.; Ihli, J.; Fielding, L. A.; Cespedes, O.; Armes, S. P.; Meldrum, F. C., One-pot synthesis of an inorganic heterostructure: uniform occlusion of magnetite nanoparticles within calcite single crystals. *Chem. Sci.* **2014,** *5*, 738.

20. Kulak, A. N.; Yang, P. C.; Kim, Y. Y.; Armes, S. P.; Meldrum, F. C., Colouring crystals with inorganic nanoparticles. *Chem. Commun.* **2014,** *50*, 67.

30. Ozgur, U.; Alivov, Y. I.; Liu, C.; Teke, A.; Reshchikov, M. A.; Dogan, S.; Avrutin, V.; Cho, S. J.; Morkoc, H., A comprehensive review of ZnO materials and devices. *J. Appl. Phys.* **2005,** 98, 041301.

31. Djurisic, A. B.; Leung, Y. H., Optical properties of ZnO nanostructures. *Small* **2006,** *2*, 944.

32. Klingshirn, C., ZnO: Material, physics and applications. *Chemphyschem* **2007,** 8, (6), 782-803.

33. Roychowdhury, A.; Pati, S. P.; Mishra, A. K.; Kumar, S.; Das, D., Magnetically addressable fluorescent Fe_3O_4/ZnO nanocomposites: Structural, optical and magnetization studies. *J. Phys. Chem. Sol.* **2013,** *74*, 811.

34. Zou, P.; Hong, X.; Chu, X. Y.; Li, Y. J.; Liu, Y. C., Multifunctional Fe_3O_4/ZnO Nanocomposites with Magnetic and Optical Properties. *J. Nanosci. Nanotech.* **2010,** *10*, 1992.

35. Bykova, L. E.; Myagkov, V. G.; Tambasov, I. A.; Bayukov, O. A.; Zhigalov, V. S.; Polyakova, K. P.; Bondarenko, G. N.; Nemtsev, I. V.; Polyakov, V. V.; Patrin, G. S.; Velikanov, D. A., Solid-state synthesis of the ZnO-Fe_3O_4 nanocomposite: Structural and magnetic properties. *Phys. Solid State* **2015,** *57*, 386.

36. Kostopoulou, A.; Thetiot, F.; Tsiaoussis, I.; Androulidaki, M.; Cozzoli, P. D.; Lappas, A., Colloidal Anisotropic ZnO-Fe@Fe_xO_y Nanoarchitectures with Interface-Mediated Exchange-Bias and Band-Edge Ultraviolet Fluorescence. *Chem. Mater.* **2012,** *24*, 2722.

37. Xia, J.; Wang, A. Q.; Liu, X.; Su, Z. X., Preparation and characterization of bifunctional, Fe_3O_4/ZnO nanocomposites and their use as photocatalysts. *Appl. Surf. Sci.* **2011,** 257, (23), 9724-9732.

38. Saffari, J.; Mir, N.; Ghanbari, D.; Khandan-Barani, K.; Hassanabadi, A.; Hosseini-Tabatabaei, M. R., Sonochemical synthesis of Fe_3O_4/ZnO magnetic nanocomposites and their application in photo-catalytic degradation of various organic dyes. *J. Mater. Sci. Mater. Elec.* **2015,** *26*, 9591.

39. Villani, M.; Rimoldi, T.; Calestani, D.; Lazzarini, L.; Chiesi, V.; Casoli, F.; Albertini, F.; Zappettini, A., Composite multifunctional nanostructures based on ZnO tetrapods and superparamagnetic Fe3O4 nanoparticles. *Nanotechnol.* **2013,** *24*, 135601.

40. Cho, N. H.; Cheong, T. C.; Min, J. H.; Wu, J. H.; Lee, S. J.; Kim, D.; Yang, J. S.; Kim, S.; Kim, Y. K.; Seong, S. Y., A multifunctional core-shell nanoparticle for dendritic cell-based cancer immunotherapy. *Nature Nanotech.* **2011,** *6*, 675.

41. Singh, S.; Barick, K. C.; Bahadur, D., Fe_3O_4 embedded ZnO nanocomposites for the removal of toxic metal ions, organic dyes and bacterial pathogens. *J. Mater. Chem. A* **2013,** *1*, 3325.

42. Wang, Z. J.; Wu, L. N.; Zhou, J. G.; Shen, B. Z.; Jiang, Z. H., Enhanced microwave absorption of Fe_3O_4 nanocrystals after heterogeneously growing with ZnO nanoshell. *RSC Adv.* **2013,** *3*, 3309.

43. Chiefari, J.; Chong, Y. K.; Ercole, F.; Krstina, J.; Jeffery, J.; Le, T. P. T.; Mayadunne, R. T. A.; Meijs, G. F.; Moad, C. L.; Moad, G.; Rizzardo, E.; Thang, S. H., Living free-radical polymerization by reversible addition-fragmentation chain transfer: The RAFT process. *Macromol.* **1998,** *31*, 5559.

44. Mandel, K.; Szczerba, W.; Thunemann, A. F.; Riesemeier, H.; Girod, M.; Sextl, G., Nitric acid-stabilized superparamagnetic iron oxide nanoparticles studied with X-rays. *J. Nano. Res.* **2012,** 14, (8).

45. Munoz-Espi, R.; Qi, Y.; Lieberwirth, I.; Gomez, C. M.; Wegner, G., Surface-functionalized latex particles as controlling agents for the mineralization of zinc oxide in aqueous medium. *Chem. Eur. J.* **2006,** *12*, 118.

46. Viswanatha, R.; Santra, P. K.; Dasgupta, C.; Sarma, D. D., Growth mechanism of nanocrystals in solution: ZnO, a case study. *Phys. Rev. Letts.* **2007,** *98*, 255501.

47. Munoz-Espi, R.; Chandra, A.; Wegner, G., Crystal perfection in zinc oxide with occluded carboxyl-functionalized latex particles. *Cryst. Growth Des.* **2006**, 1584.

48. Sykes, G. A.; Collins, M. J.; Walton, D. I., The significance of a geochemically isolated intracrystalline organic fraction within biominerals. *Org. Geochem.* **1995,** 23, (11-12), 1059.

49. Guo, S. X.; Du, Z. L.; Da, S. X., Analysis of Raman modes in Mn-doped ZnO nanocrystals. *Phys. Status Solidi B* **2009,** 246, (10), 2329.

50. Hanesch, M., Raman spectroscopy of iron oxides and (oxy)hydroxides at low laser power and possible applications in environmental magnetic studies. *Geophys. J. Int.* **2009,** 177, (3), 941.

51. deFaria, D. L. A.; Silva, S. V.; deOliveira, M. T., Raman microspectroscopy of some iron oxides and oxyhydroxides. *J. Raman Spec.* **1997,** 28, (11), 873.

52. Bojesen, E. D.; Jensen, K. M. O.; Tyrsted, C.; Lock, N.; Christensen, M.; Iversen, B. B., In Situ Powder Diffraction Study of the Hydrothermal Synthesis of ZnO Nanoparticles. *Cryst. Growth Des.* **2014,** *14*, 2803.

53. Goya, G. F.; Berquo, T. S.; Fonseca, F. C.; Morales, M. P., Static and dynamic magnetic properties of spherical magnetite nanoparticles. *J. Appl. Phys.* **2003,** *94*, 3520.

54. Tamion, A.; Raufast, C.; Hillenkamp, M.; Bonet, E.; Jouanguy, J.; Canut, B.; Bernstein, E.; Boisron, O.; Wernsdorfer, W.; Dupuis, V., Magnetic anisotropy of embedded Co nanoparticles: Influence of the surrounding matrix. *Phys. Rev. B* **2010,** *81*, 144403.

55. Mishra, Y. K.; Mohapatra, S.; Singhal, R.; Avasthi, D. K.; Agarwal, D. C.; Ogale, S. B., Au-ZnO: A tunable localized surface plasmonic nanocomposite. *Appl. Phys. Letts.* **2008,** 92, 043107.

56. Zheng, Y. H.; Zheng, L. R.; Zhan, Y. Y.; Lin, X. Y.; Zheng, Q.; Wei, K. M., Ag/ZnO heterostructure nanocrystals: Synthesis, characterization, and photocatalysis. *Inorg. Chem.* **2007,** *46*,, 6980.

57. Lu, W. W.; Gao, S. Y.; Wang, J. J., One-Pot Synthesis of Ag/ZnO Self-Assembled 3D Hollow Microspheres with Enhanced Photocatalytic Performance. *J. Phys. Chem. C* **2008,** *112*, 16792.

58. Bian, Z. F.; Tachikawa, T.; Zhang, P.; Fujitsuka, M.; Majima, T., A nanocomposite superstructure of metal oxides with effective charge transfer interfaces. *Nature Commun.* **2014,** *5*, 3038.

59. Wu, W.; Zhang, S. F.; Xiao, X. H.; Zhou, J.; Ren, F.; Sun, L. L.; Jiang, C. Z., Controllable Synthesis, Magnetic Properties, and Enhanced Photocatalytic Activity of Spindlelike Mesoporous alpha-Fe_2O_3/ZnO Core-Shell Heterostructures. *ACS Appl. Mater. Int.* **2012,** *4*, 3602.

60. Liu, M. H.; Chen, Y. W.; Liu, X. Y.; Kuo, J. L.; Chu, M. W.; Mou, C. Y., Defect-Mediated Gold Substitution Doping in ZnO Mesocrystals and Catalysis in CO Oxidation. *ACS Catal.* **2016,** *6*, 115.

61. Kahr, B.; Gurney, R. W., Dyeing crystals. *Chem. Rev.* **2001,** *101*, 893.

62. Li, H. Y.; Xin, H. L.; Kunitake, M. E.; Keene, E. C.; Muller, D. A.; Estroff, L. A., Calcite Prisms from Mollusk Shells (Atrina Rigida): Swiss-cheese-like Organic-Inorganic Single-crystal Composites. *Adv. Func. Mater.* **2011,** *21*, 2028.

63. Kim, Y. Y.; Carloni, J. D.; Demarchi, B.; Sparks, D.; Reid, D. G.; Kunitake, M. E.; Tang, C. C.; Duer, M. J.; Freeman, C. L.; Pokroy, B.; Penkman, K.; Harding, J. H.; Estroff, L. A.; Baker, S. P.; Meldrum, F. C., Tuning hardness in calcite by incorporation of amino acids *Nature Mater.* **2016,** *15*, 903.

64. Borukhin, S.; Bloch, L.; Radlauer, T.; Hill, A. H.; Fitch, A. N.; Pokroy, B., Screening the Incorporation of Amino Acids into an Inorganic Crystalline Host: the Case of Calcite. *Adv. Func. Mater.* **2012,** *22*, 4216.

65. Brif, A.; Ankonina , G.; Drathen , C.; Pokroy, B., Bio-Inspired Band Gap Engineering of Zinc Oxide by Intracrystalline Incorporation of Amino Acids. *Adv. Mater.* **2014,** *26*, 477.

66. Chien, Y. C.; Masica, D. L.; Gray, J. J.; Nguyen, S.; Vali, H.; McKee, M. D., Modulation of Calcium Oxalate Dihydrate Growth by Selective Crystal-face Binding of Phosphorylated Osteopontin and Polyaspartate Peptide Showing Occlusion by Sectoral (Compositional) Zoning. *J. Biol. Chem.* **2009,** *284*, 23491.

67. Ning, Y.; Fielding, L. A.; Andrews, T. S.; Growney, D. J.; Armes, S. P., Sulfate-based anionic diblock copolymer nanoparticles for efficient occlusion within zinc oxide. *Nanoscale* **2015,** *7*, 6691.

68. Cho, K.-R.; Kim, Y.-Y.; Yang, P.; Cai, W.; Pan, H.; Kulak, A. N.; Lau, J. L.; Kulshreshtha, P.; Armes, S. P.; Meldrum, F. C.; De Yoreo, J. J., Direct observation of mineral-organic composite formation reveals occlusion mechanism. *Nature Commun.* **2015,** *7*, 10187.

69. Ricci, M.; Segura, J. J.; Erickson, B. W.; Fantner, G.; Stellacci, F.; Voitchovsky, K., Growth and Dissolution of Calcite in the Presence of Adsorbed Stearic Acid. *Langmuir* **2015,** *31*, 7563.

70. De Yoreo, J. J.; Gilbert, P.; Sommerdijk, N.; Penn, R. L.; Whitelam, S.; Joester, D.; Zhang, H. Z.; Rimer, J. D.; Navrotsky, A.; Banfield, J. F.; Wallace, A. F.; Michel, F. M.; Meldrum, F. C.; Colfen, H.; Dove, P. M., Crystallization by particle attachment in synthetic, biogenic, and geologic environments. *Science* **2015,** *349*, doi: 10.1126/science.aaa6760.

71. Ludi, B.; Niederberger, M., Zinc oxide nanoparticles: chemical mechanisms and classical and non-classical crystallization. *Dalton Trans.* **2013,** *42*, 12554.

72. Liu, Y. X.; Wang, D. S.; Peng, Q.; Chu, D. R.; Liu, X. W.; Li, Y. D., Directly Assembling Ligand-Free ZnO Nanocrystals into Three-Dimensional Mesoporous Structures by Oriented Attachment. *Inorg. Chem.* **2011,** *50*, 5841.

73. Liu, M. H.; Tseng, Y. H.; Greer, H. F.; Zhou, W. Z.; Mou, C. Y., Dipole Field Guided Orientated Attachment of Nanocrystals to Twin-Brush ZnO Mesocrystals. *Chem. Eur. J.* **2012,** *18*, 16104.

74. Feng, W. L.; Huang, P., A generalized mechanism of 1D ZnO rods growth in homogeneous solution. *Ceram. Int.* **2014,** *40*, 8963.

75. Berman, A.; Hanson, J.; Leiserowitz, L.; Koetzle, T.; Weiner, S.; Addadi, L., Crystal-protein interactions: controlled anisotropic changes in crystal microtexture. *J. Phys. Chem.* **1993,** *97*, 5162.

76. Asenath-Smith, E.; Li, H. Y.; Keene, E. C.; Seh, Z. W.; Estroff, L. A., Crystal Growth of Calcium Carbonate in Hydrogels as a Model of Biomineralization. *Adv. Func. Mater.* **2012,** *22*, 2891.

77. Kulak, A. N.; Grimes, R.; Kim, Y.-Y.; Semsarilar, M.; Anduix-Canto, C.; Cespedes, O.; Armes, S. P.; Meldrum, F. C., Dataset for Polymer-Directed Assembly of Single Crystal Zinc Oxide/ Magnetite Nanocomposites under Atmospheric and Hydrothermal Conditions. *Research Data Leeds Repository* **2016**, http://doi.org/xxx.

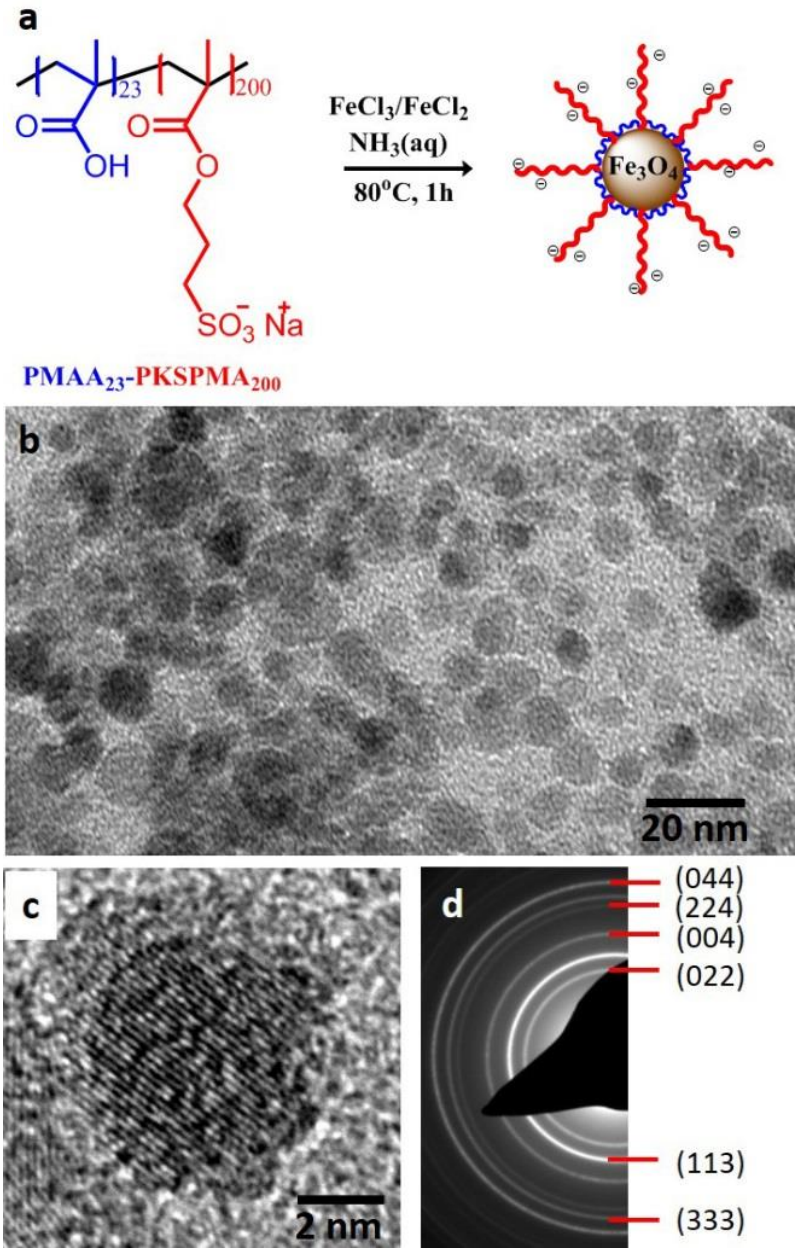

Figure 1. (a) Scheme describing the preparation of Fe_3O_4 magnetic nanoparticles stabilized by $PMAA_{23}$-$PKSPMA_{200}$ (MNPs), (b) TEM image of magnetite nanoparticles (c) high resolution TEM image of an individual nanoparticle and (d) selected area electron diffraction pattern of magnetite nanoparticles.

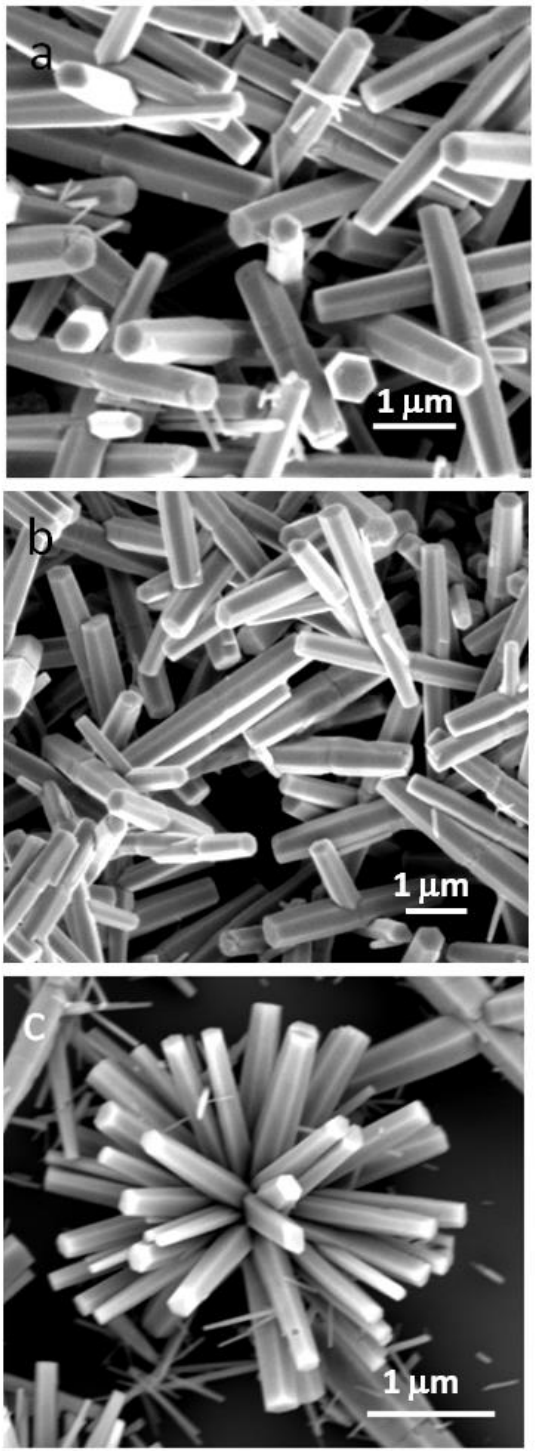

Figure 2. SEM images of ZnO crystals precipitated from aqueous solution at 90 °C, from reagent solutions of concentrations [Zn^{2+}] = [HMTA] = (a) 0.5 mM, (b) 1 mM and (c) 1.5 mM.

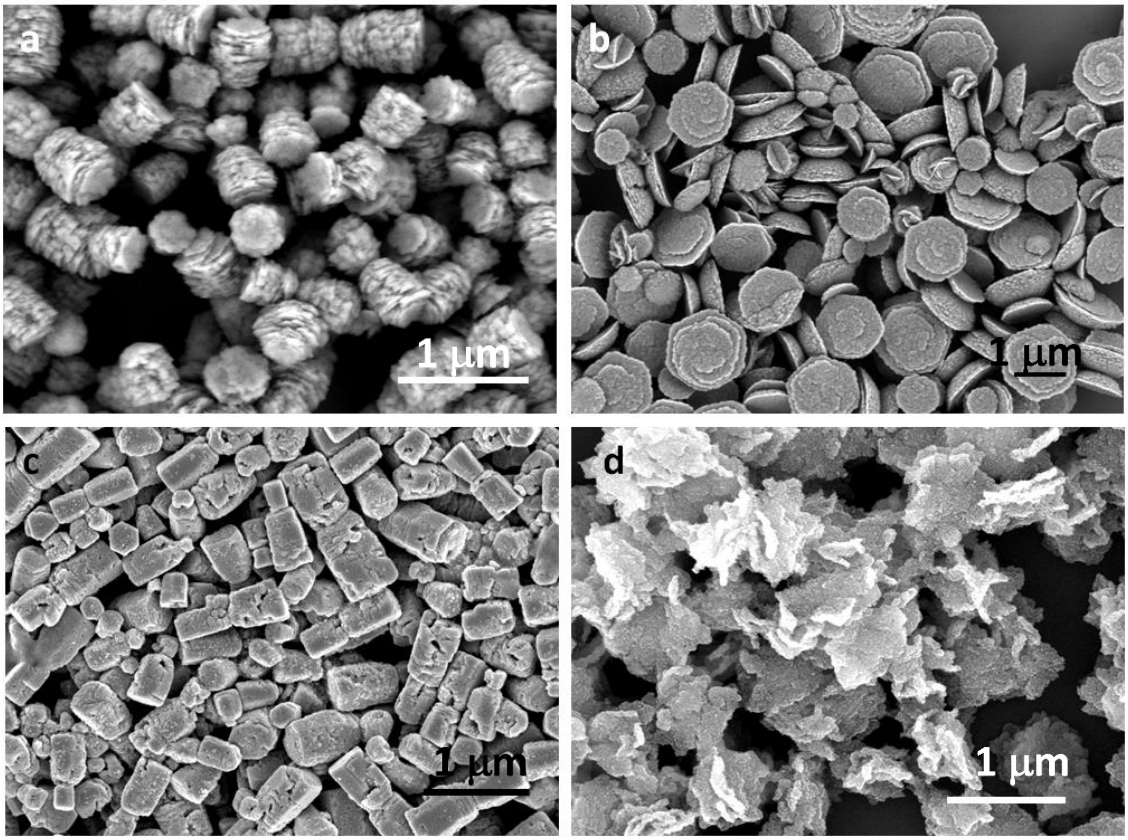

Figure 3. SEM images of ZnO crystals precipitated in the presence of PS-MNPs from aqueous solution at 90 ^{o}C. (a) Reagent solutions of [Zn^{2+}] = [HMTA] = 0.5 mM, and 0.168 μg mL^{-1} PS-MNPs, (b) [Zn^{2+}] = [HMTA] = 0.5 mM, and 0.504 μg mL^{-1} PS-MNPs, (c) [Zn^{2+}] = [HMTA] = 1 mM, and 0.168 μg mL^{-1} PS-MNPs and (d) [Zn^{2+}] = [HMTA] = 1.5 mM, and 0.504 μg mL^{-1} PS-MNPs.

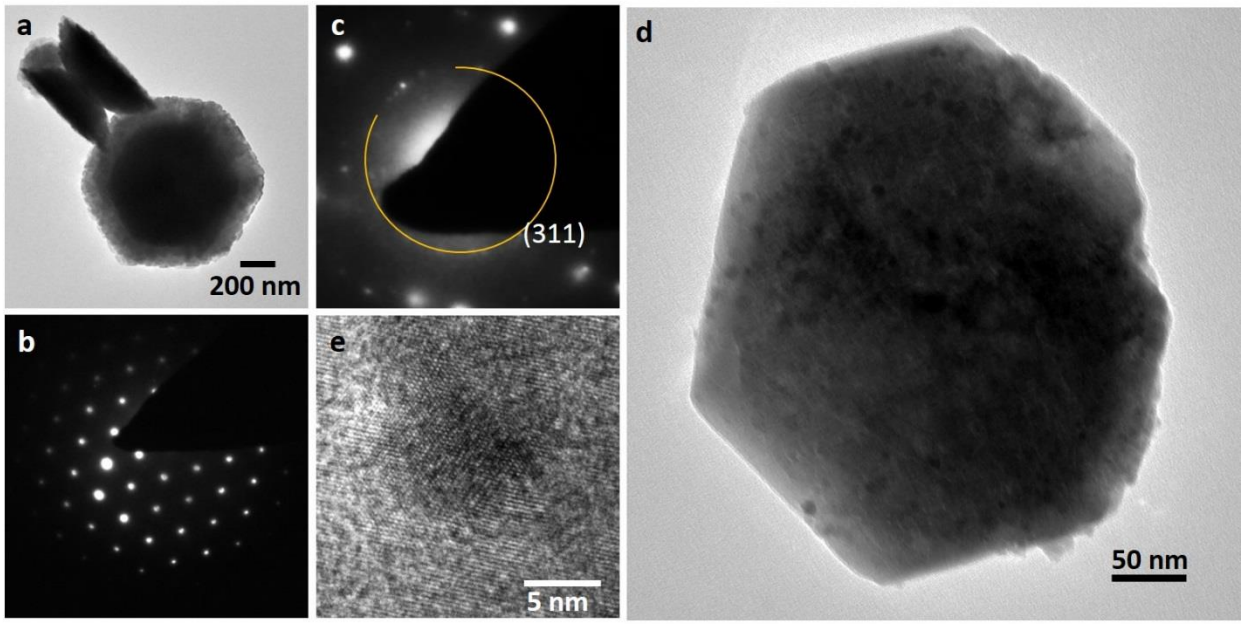

Figure 4. TEM micrographs of ZnO/PS-MNP nanocomposite crystals precipitated from aqueous solution at 90 ^{o}C. (a) Typical image of particles showing a hexagonal cross section and double-barrelled morphology, (b and c), selected area diffraction patterns of a ZnO/PS-MNP nanocomposite crystal corresponding to single crystal wurzite (zone axis 001) (c) after tilting off-axis, rings/spots corresponding to the (311) reflection of magnetite can be observed. (d) TEM image of MNPs distributed throughout the ZnO crystal. (e) A high resolution TEM image of magnetite nanoparticles within the continuous lattice of ZnO.

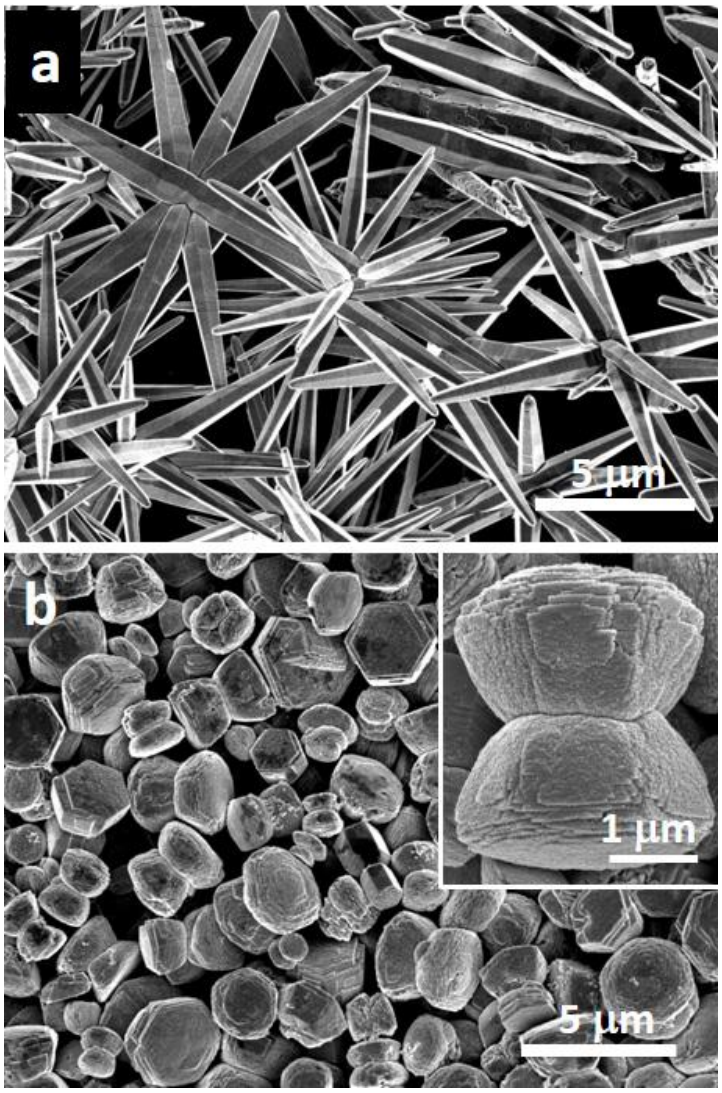

Figure 5. (a and b) SEM images of ZnO crystals prepared using a hydrothermal method at 160 °C for 12 h with $[Zn^{2+}]$ = [HMTA] = 5 mM (a) in the absence of PS-MNPs, and (b) in the presence of 3.36 µg mL^{-1} PS-MNPs.

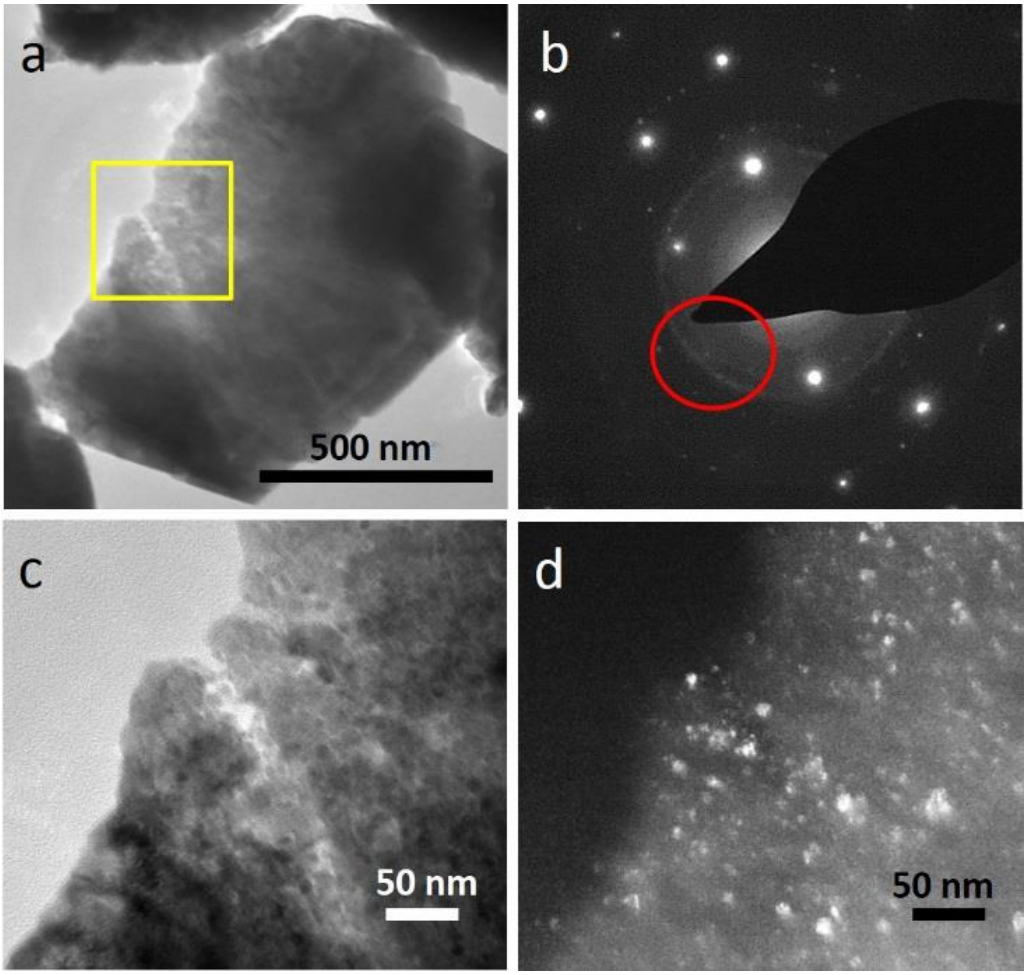

Figure 6. TEM analysis of ZnO/PS-MNP nanocomposite crystal prepared using a hydrothermal method at 160 °C for 12 h with $[Zn^{2+}]$ = [HMTA] = 5 mM in the presence of 3.36 μg mL^{-1} PS-MNPs, where (a) a flake thin enough for analysis was prepared by grinding. (b) Selected area electron diffraction pattern of the area shown be a yellow square in (a), showing a single crystal pattern corresponding to ZnO and rings corresponding to magnetite. (c) Bright field TEM image of the area in the yellow box and (d) corresponding dark field image of the same area, in which the diffracting MNPs (the circled rings were selected) appear bright.

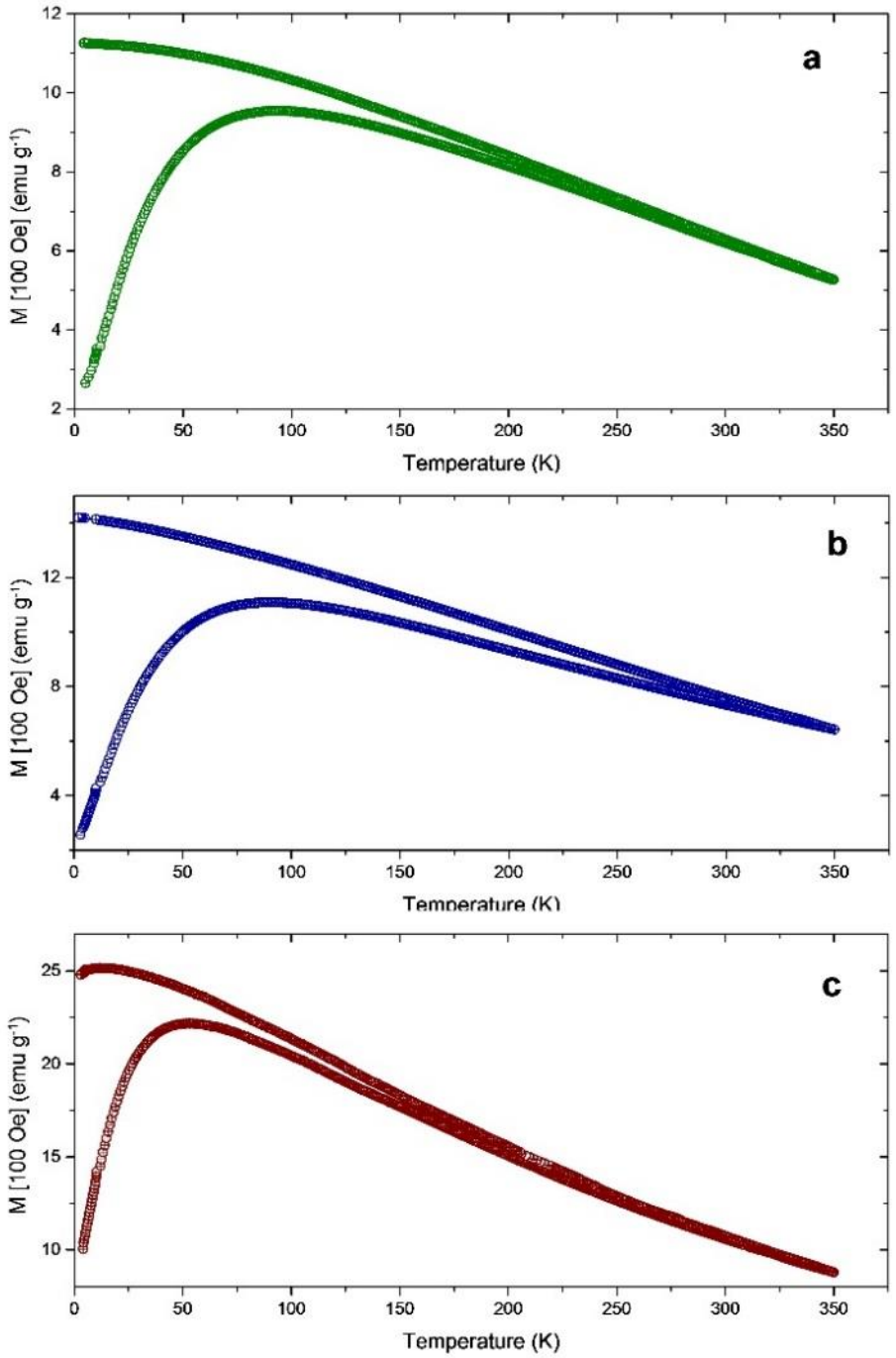

Figure 7. Thermomagnetic zero-field-cooled/field-cooled (ZFC/ FC) curves of (a) PS-MNPs, (b) ZnO/PS-MNP crystals prepared under standard conditions and (c) ZnO/PS-MNP crystals prepared under hydrothermal conditions. The magnetization values are given wrt to the amount of magnetite present in each sample.

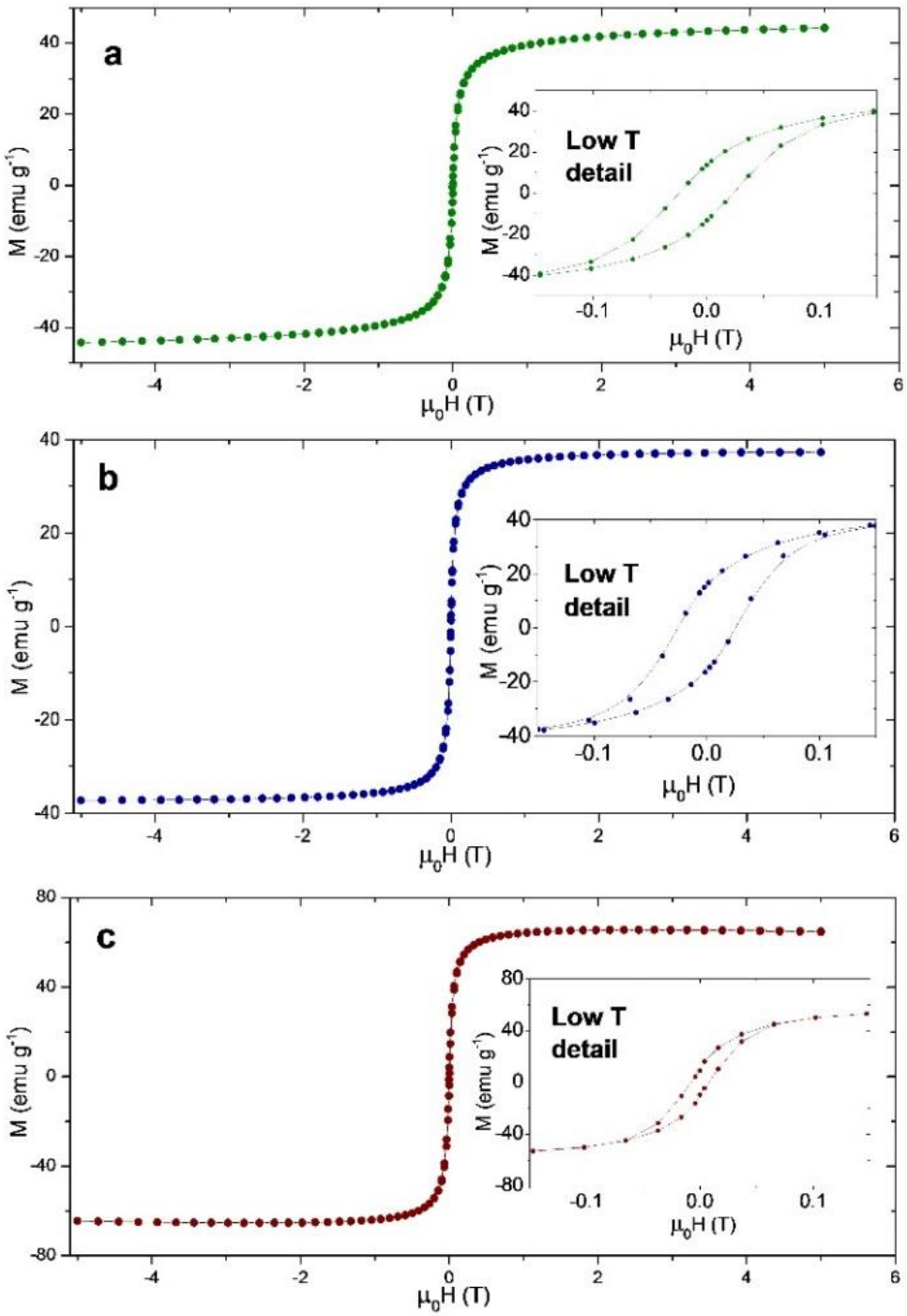

Figure 8. (a) Magnetization loops measured at 300 K and low temperature (insets) of (a) PS-MNPs, (b) ZnO/PS-MNP crystals prepared under standard conditions and (c) ZnO/PS-MNP crystals prepared under hydrothermal conditions. The magnetization values are given wrt to the amount of magnetite present in each sample